Atmos. Meas. Tech. Discuss., 7, 11991–12036, 2014
www.atmos-meas-tech-discuss.net/7/11991/2014/
doi:10.5194/amtd-7-11991-2014

Atmospheric Measurement Techniques Discussions
Open Access

Cloud thermodynamic phase detection with polarimetrically sensitive passive sky radiometers

K. Knobelspiesse[1], B. van Diedenhoven[2], A. Marshak[3], S. Dunagan[1], B. Holben[3], and I. Slutsker[4]

[1]NASA Ames Research Center, Moffett Field, CA, USA
[2]Columbia University and NASA Goddard Institute for Space Studies, New York, NY, USA
[3]NASA Goddard Space Flight Center, Greenbelt, MD, USA
[4]Sigma Space Corporation and NASA Goddard Space Flight Center, Greenbelt, MD, USA

Received: 21 October 2014 – Accepted: 4 November 2014 – Published: 2 December 2014

Correspondence to: K. Knobelspiesse (kirk.knobelspiesse@nasa.gov)

Published by Copernicus Publications on behalf of the European Geosciences Union.

Abstract

The primary goal of this project has been to investigate if ground-based visible and near-infrared passive radiometers that have polarization sensitivity can determine the thermodynamic phase of overlying clouds, i.e. if they are comprised of liquid droplets or ice particles. While this knowledge is important by itself for our understanding of the global climate, it can also help improve cloud property retrieval algorithms that use total (unpolarized) radiance to determine Cloud Optical Depth (COD). This is a potentially unexploited capability of some instruments in the NASA Aerosol Robotic Network (AERONET), which, if practical, could expand the products of that global instrument network at minimal additional cost.

We performed simulations that found, for zenith observations, cloud thermodynamic phase is often expressed in the sign of the Q component of the Stokes polarization vector. We chose our reference frame as the plane containing solar and observation vectors, so the sign of Q indicates the polarization direction, parallel (positive) or perpendicular (negative) to that plane. Since the quantity of polarization is inversely proportional to COD, optically thin clouds are most likely to create a signal greater than instrument noise. Besides COD and instrument accuracy, other important factors for the determination of cloud thermodynamic phase are the solar and observation geometry (scattering angles between 40 and 60° are best), and the properties of ice particles (pristine particles may have halos or other features that make them difficult to distinguish from water droplets at specific scattering angles, while extreme ice crystal aspect ratios polarize more than compact particles).

We tested the conclusions of our simulations using data from polarimetrically sensitive versions of the Cimel 318 sun photometer/radiometer that comprise AERONET. Most algorithms that exploit Cimel polarized observations use the Degree of Linear Polarization (DoLP), not the individual Stokes vector elements (such as Q). For this reason, we had no information about the accuracy of Cimel observed Q and the potential for cloud phase determination. Indeed, comparisons to ceilometer observations

AMTD
7, 11991–12036, 2014

with a single polarized spectral channel version of the Cimel at a site in the Netherlands showed little correlation. Comparisons to Lidar observations with a more recently developed, multi-wavelength polarized Cimel in Maryland, USA, show more promise. The lack of well characterized observations has prompted us to begin the development of a small test instrument called the Sky Polarization Radiometric Instrument for Test and Evaluation (SPRITE). This instrument is specifically devoted to the accurate observation of Q, and the testing of calibration and uncertainty assessment techniques, with the ultimate goal of understanding the practical feasibility of these measurements.

1 Introduction

The relationship between clouds and aerosols have long been recognized as one of the least certain components of the global climate, largely due to the difficulty of acquiring relevant global datasets (IPCC, 2013). This was the motivation for the establishment of the NASA Aerosol Robotic Network (AERONET), which is chiefly devoted to the measurement of atmospheric aerosols by the use of sun photometer/sky radiometers manufactured by Cimel, Inc. (Holben et al., 1998). These instruments typically "sleep" when clouds obscure the sun, but select instruments also collect data while pointed in the zenith direction. Data collected in this "cloud mode" are used to determine Cloud Optical Depth (COD) and cloud fraction (Marshak et al., 2000, 2004; Barker and Marshak, 2001; Chiu et al., 2006, 2010). This algorithm relies on the spectral contrast between blue and near-infrared (or red) reflectances of vegetated surfaces surrounding the measurement site, and employs a Lookup Table (LUT) of precomputed radiances to match observations to retrieved parameters. These LUT's are generated for a cloud with a known thermodynamic phase, liquid or ice, and the use of the incorrect LUT can lead to very large retrieval errors. For example, recent cloud observations during the DRAGON (Distributed Regional Aerosol Gridded Observation Networks) field campaign were consistent with a COD of 18 for an ice phase cloud, but 30 for a water phase cloud (S. Huang, personal communication, 2012). Since this uncertainty significantly

AMTD
7, 11991–12036, 2014

impacts our ability to improve climate models, we have searched for methods to determine cloud thermodynamic phase from instrument operating in "cloud mode".

A portion of the Cimel instruments used by AERONET are sensitive to linearly polarized radiation. These clear sky measurements are primarily used to determine aerosol optical properties (Li et al., 2004, 2006, 2007, 2009, 2010, 2013). Our goal is to determine if polarimetric observations made by AERONET instruments operating in the "cloud mode" can also be used to identify cloud thermodynamic phase, and therefore improve the retrieval of cloud properties by selecting the proper LUT. This paper is subsequently divided into three main sections. The next section (Sect. 2) describes the results of vector radiative transfer simulations of ice and liquid phase clouds as observed by ground radiometers such as the Cimels employed by AERONET. Section 3 contains an analysis of actual AERONET polarized cloud observations and comparison to independent datasets that serve as proxies to cloud thermodynamic phase. Section 4 discusses the previous two sections and makes recommendations for future observations. We conclude in Sect. 5. Additionally, Appendix A provides an uncertainty analysis for these types of measurements.

2 Simulations

We began by performing simulations of a cloud-atmosphere system, utilizing a vector (polarimetric) radiative transfer model developed at NASA Goddard Institute for Space Studies (GISS). This model uses the Doubling and Adding technique to compute multiple scattering in a plane parallel system (de Haan et al., 1987). Single scattering properties were computed as the Lorenz-Mie solution of Maxell's equations (Hansen and Travis, 1974) for spherical liquid water droplets, or for randomly oriented, "roughened" hexagonal ice plates or columns using geometric optics (Macke et al., 1996). Figure 1 is a cartoon describing the simulated scenes, which were performed at a variety of COD's (2.5, 5, 7.5, 10, 15, 20 and 30) and Solar Zenith Angles (SZA, 15, 30, 45 and 60°). Ice phase clouds, which were lofted between 7 and 7.5 km in a standard atmosphere, were

AMTD
7, 11991–12036, 2014

simulated with ice particle aspect ratios (the ratio of height to width) of 0.05, 1, 2 and 20 and roughness parameters (Macke et al., 1996) of 0 (pristine) and 0.4. Although natural clouds generally contain more complex ice crystals, the scattering properties of single hexagonal prisms closely resemble those of such complex structures (Baran, 2009; Um and McFarquhar, 2007, 2009; van Diedenhoven et al., 2014). Since ice clouds can be simulated with geometric scattering for visible and near infrared wavelengths, particle size is minimally relevant for fixed COD. Liquid phase clouds were simulated at lower altitudes (between 1.5 and 3 km) for droplets with effective radii of 10 and 5 µm. To correspond with AERONET instrument spectral sensitivity, these simulations were performed at 440, 500, 560, 675, 870 and 1020 nm. These channels were also chosen so that they are minimally affected by atmospheric gas absorption. Total column pressure was 1013.25 mb, and ground temperature 288.15 °K. COD retrieval from "cloud mode" radiometers uses the spectral contrast of surface reflectance, which works best when that surface is very "green", expressed as a high Normalized Difference Vegetation Index (NDVI). We therefore chose a surface spectral reflectance from vegetated surface measurements in late summer central Oklahoma (Knobelspiesse et al., 2008). To test the sensitivity to these model conditions, we also performed simulations with modified altitude profiles and surface reflectances, and individually simulated a cloud with mixed liquid and ice phase.

Simulation results were expressed as the Stokes' polarization vector, $\boldsymbol{I} = [I, Q, U, V]$, observed by a noiseless, upwards looking radiometer at the ground. We present these values as unitless, and equivalent to reflectance that would be observed by a downwards looking instrument, i.e.

$$\boldsymbol{R} = \frac{\boldsymbol{I}\pi r_o^2}{F_o \cos\theta_s} \tag{1}$$

where $\boldsymbol{I}$ is the Stokes' vector in radiance ($\mathrm{W\,m^{-2}\,sr^{-1}}$), r_o is the solar distance in astronomical units (AU) (we used $r_o = 1$), F_o is the exo-atmospheric irradiance ($\mathrm{W\,m^{-2}}$) at a solar distance of AU = 1, and θ_s is the Solar Zenith Angle. Generally speaking, the

AMTD
7, 11991–12036, 2014

I component of the Stokes' vector expresses the total reflectance, Q and U express the magnitude and direction of linear polarization, and V the circular polarization. For scattered solar light in the atmosphere at visible and near-infrared wavelengths, V is small ($< 0.2\%$ of linear polarization, de Haan et al., 1987; Kawata, 1978), so we restrict ourselves in this analysis to the first three Stokes' vector elements, [I, Q, U]. This subset of the Stokes' vector is also relatively simple to observe, and is easily obtained from direct measurements. The Cimel radiometers use linearly polarizing filters at different orientations, so that the linearly polarizing component of the Stokes' vector is computed

$$\boldsymbol{I} = \begin{bmatrix} I \\ Q \\ U \end{bmatrix} = \begin{bmatrix} \frac{2}{3}\left(\hat{I}(0^\circ) + \hat{I}(120^\circ) + \hat{I}(240^\circ)\right) \\ \frac{2}{3}\left(2\hat{I}(0^\circ) - \hat{I}(120^\circ) - \hat{I}(240^\circ)\right) \\ \frac{2}{\sqrt{3}}\left(\hat{I}(240^\circ) - \hat{I}(120^\circ)\right) \end{bmatrix} \quad (2)$$

where $\hat{I}(X)$ indicates the radiance observed in a Cimel channel with a linear polarizer oriented at X° from the reference plane (which is typically chosen at the solar principal plane, containing both the solar illumination and observation direction vectors) (Chandrasekhar, 1960).

A common polarization metric is the Degree of Linear Polarization (DoLP),

$$\mathrm{DoLP} = \frac{\sqrt{Q^2 + U^2}}{I} = \frac{\sqrt{R_Q^2 + R_U^2}}{R_I} \quad (3)$$

which is used as a means to represent the quantity of linear polarization in a scene independent of reference frame. This presents an advantage because of simplicity and diminished sensitivity to calibration uncertainty and errors in filter orientation (X), but also means information about polarization direction has been discarded. As we shall see, polarization direction most clearly expresses cloud thermodynamic phase, so we are compelled to avoid DoLP.

AMTD
7, 11991–12036, 2014

2.1 Simulation results

Figure 2 is an example of the typical polarization encountered with water (solid) and ice (dashed) clouds as observed by a narrow Field of View (FOV) ground radiometer at a variety of zenith angles in the solar principal plane. I is generally at least an order of magnitude larger than DoLP or Q (note the axes). There are no systematic (for different clouds) distinctions between water and ice phase clouds in I or DoLP, especially for zenith observations. However, the Q of water and ice clouds have opposite signs at most angles, meaning that polarization direction differs. For these reasons, we believe Q is the best means to determine cloud thermodynamic phase when defined in the solar principal plane as it is here. U is many orders of magnitude smaller than DoLP or Q, meaning that it contains little information about clouds. As we shall see later, we use this property of U to ensure that we have properly identified the solar principal plane. We could, of course, also describe the polarization direction by the polarization angle, $\chi = \frac{1}{2}\tan^{-1}(U/Q)$. The convention from Hansen and Travis (1974) for χ is to select the value in the interval $0 \leq \chi < \pi$ where the sign of $\cos(2\chi)$ and Q are the same. Because uncertainty and numerical issues are easier to track, we will express the results of our simulations and analysis in Q.

The polarization direction difference between liquid and ice phase clouds is inherent to the single scattering properties of water droplets and ice crystals. We can see this by plotting the P_{11} and P_{12} phase matrix elements, as we have done in Fig. 3. The phase matrix, $\mathbf{P}$ transforms an incoming wave of radiation (such as unpolarized solar radiation, $\boldsymbol{I}_o = [1,0,0,0]$) to the scattered wave at a scattering angle, γ, such that

$$\boldsymbol{I}(\gamma) = k_e \varpi \frac{dv}{4\pi R^2} \mathbf{P}(\gamma) \boldsymbol{I}_o \tag{4}$$

where dv is the scattering volume, k_e is the extinction coefficient, ϖ is the single scattering albedo (the ratio of scattering to total extinction) and R is the distance from dv to the observation location. Thus, the P_{11} element describes the transfer from I_o to I, while P_{12} the transfer of I_o to Q. Figure 3 shows us that, at scattering angles relevant

AMTD
7, 11991–12036, 2014

to ground observation (roughly $10^\circ < \gamma < 70^\circ$), liquid and ice phase clouds are not dramatically different for P_{11}, but have different sign for P_{12}.

Figure 4 shows the type of measurements that ground based, zenith viewing polarimeters would make of ice and liquid clouds with various COD. The Q Stokes vector element, at left, clearly expresses the distinction between liquid and ice phase clouds. The reference frame defining Q is the solar principal plane, where the value of U is very small. The DoLP, at right, is nearly equivalent to the absolute value of Q, so the distinction between water and ice phase is lost. Both Q and DoLP show the most polarization for the smallest COD, meaning that the ability to determine thermodynamic phase diminishes for thicker clouds. We can also see that the largest (negative) polarization for ice clouds is generated for crystals with the most extreme Aspect Ratio (AR). Based on so-called "directional memory", the original radiative direction is lost after $1/(1-g)$ orders of scattering, and thereafter travels isotropically (Davis and Marshak, 2002) (here, g is the asymmetry factor, the first moment of the P_{11} phase matrix element). If we assume a multiplicative coefficient of proportionality of 2, and a liquid cloud $g = 0.85$, the optical depth associated with the loss of directional memory occurs at $\frac{2}{1-g} = \frac{2}{1-0.85} = 13.3$ or greater. Figure 4 is consistent with this relationship, since Q and DoLP, as expressions of directionality, converge to zero for roughly COD > 13.

2.2 Observability

Figure 4 makes a compelling case for the observability of cloud thermodynamic phase with polarization, but several factors affect the ability to make this distinction with real observations. Instrument uncertainty is of utmost importance, yet often remains uncharacterized for Q and U (Appendix A is an uncertainty characterization of an instrument that uses linearly polarizing filters, such as the Cimel radiometers used by AERONET). Geophysical characteristics of the scene are also important. Factors such as the solar zenith angle (or more directly, the scattering angle) play a role, and the presence of halos or other features of pristine ice crystals can also interfere with with cloud phase determination. On the other hand, factors which are typically important

AMTD
7, 11991–12036, 2014

for remote sensing of clouds from the ground, such as the need to account for nearby surface reflectance and cloud base height, are relatively unimportant.

Figure 5 shows the scattering angle dependence of Q at 870 nm for liquid and ice clouds for a variety of simulated solar zenith angles. Here, we define scattering angle as the angle between the solar illumination direction and the scattered direction. Results from simulations with a variety of solar zenith angles show similar behavior, indicating that the scattering angle largely defines Q. The liquid cloud is most polarizing at scattering angles roughly between 40 and 50°, while ice clouds are most (negatively) polarizing at angles between 60 and 70°. Differentiation between liquid and ice clouds is therefore best performed in this range, where scattering angles are between 40 and 70°. For zenith measurements, the solar zenith angle is the scattering angle, meaning that phase differentiation is best when solar zenith angle is between 40 and 70°, and improbable when it is less than 20°. If a ground based radiometer has the ability to control pointing direction, the optimal measurement would not necessarily be made at zenith, but in a direction in the solar principal plane roughly 55° from the sun.

The linearly polarized scattering of ice crystals (P_{12}, the right panel in Fig. 3) is primarily dependent upon AR and surface roughness (randomization of scattering) (van Diedenhoven et al., 2012). Ice crystals are generally large enough for their scattering properties to be simulated with geometric optics (Bi et al., 2014), so size has a minimal impact on P_{12}. Since cloud chamber, in situ and remote sensing observations indicate that distorted, roughened ice crystals are generally prevalent (Baran, 2009; van Diedenhoven et al., 2013; Pfalzgraff et al., 2010; Magee et al., 2014), we have performed our simulations with crystals that have been roughened. However, pristine ice crystals do exist in clouds, as is indicated by the frequent observation of halos from the ground (Sassen et al., 2003; van Diedenhoven, 2014). Observations performed at some combinations of viewing and solar zenith angles mean that these halos would be directly measured. As is shown in Fig. 6, the halo value of Q spikes above zero, meaning that it looks similar to liquid phase clouds. Lacking other observations, ice clouds at this geometry would be confused for liquid phase clouds. From

AMTD
7, 11991–12036, 2014

a measurementperspective, the halo at 46° is potentially the most problematic, since the 22° halo is already at a scattering angle where it is difficult to distinguish liquid from ice clouds. However, the 46° halo is very rarely observed, and only occurs when the cloud is comprised of a large fraction of pristine particles (van Diedenhoven, 2014). Furthermore, the simulation of totally pristine crystals shown here must be considered as a limiting case, since some level of distortion or roughening is likely for crystals in most halo-producing cirrus clouds (Shcherbakov, 2013; van Diedenhoven, 2014).

The spectral dependance for selected visible and near-infrared channels (corresponding to multiple polarized channel Cimel wavelengths) are shown in Fig. 7. As we can see, the cloud thermodynamic phase linear polarization direction effect (expressed as Q) is largely preserved at different wavelengths. Generally, Q decreases as wavelength decreases, such that Q (440 nm) for liquid phase clouds are less than zero in the most extreme case. Simulations of liquid clouds comprised by other size droplets are nearly identical to the single liquid cloud shown in the figure, while different aspect ratio ice clouds show similar spectral dependence but varying absolute magnitudes of Q (similar to what is shown in Fig. 4).

For both ice and liquid clouds, observations of Q are insensitive to factors that typically affect I, such as cloud vertical distribution and surface reflectance. This is illustrated in Fig. 8, where these properties have been modified, and have no noticeable effect on Q. I, in contrast, is quite sensitive to surface reflectance, particularly at 870 nm, where vegetated surfaces can be quite bright. In fact, this forms the basis of the cloud optical depth retrieval algorithms used by AERONET (Chiu et al., 2006, 2010). The sensitivity to vertical distribution increases with increased Rayleigh scattering at shorter wavelengths, but the impact of this on Q remains minimal.

We also performed simulations for mixed phase clouds. Figure 9 shows the transition from negative to positive values of nadir observed Q for a cloud with liquid on the bottom and ice on the top. While this transition is gradual, it should be noted that the cloud with 50 % liquid and 50 % ice has negative values of Q for all simulated values of total COD.

AMTD
7, 11991–12036, 2014

If the sign of Q is used to identify cloud thermodynamic phase, this cloud would be identified as one comprised of ice.

To conclude, we have simulated a variety of ice and liquid phase clouds, and found that the linear polarization direction, expressed as the sign of the Q element of the Stokes polarization vector (defined in the scattering plane), indicates thermodynamic phase. The utility of this distinction is dependent upon the total COD (thinner clouds polarize more), the solar and observational viewing geometry (scattering angles between 40 and 70° are best), ice crystal aspect ratio (values close to AR = 1.0 polarize least), and the instrument accuracy with respect to Q. Additionally, the ability to determine cloud thermodynamic phase with polarization is insensitive to the altitude of the cloud or the surface reflectance.

There are many ways to determine cloud thermodynamic phase from the ground, such as with active measurements (Sassen, 1991), spectral ratios (Martins et al., 2011; LeBlanc et al., 2014) and microwave radiometers (Turner et al., 2003; Shupe et al., 2005; Campos et al., 2014, for example). This method generally may not be as powerful as those techniques, but in certain conditions (such as low COD) it may be more sensitive, which also means that it is affected by different portions of the cloud vertical profile. It also can be performed by AERONET instruments when they observe clouds, with no modification other than to measurement protocol. AERONET instruments have been deployed in hundreds of locations throughout the world for more than a decade (Holben et al., 1998), and our simulations show that data from the polarized instruments in the network could potentially provide information on cloud thermodynamic phase as well.

3 Data exploration

We tested our simulations with AERONET Cimel data collected at two sites that have co-located independent observations of proxies to cloud thermodynamic phase. Each site employed a different version of the Cimel instrument. An early variant of the

AMTD
7, 11991–12036, 2014

instrument, which has polarization sensitivity in a single channel centered at 870 nm, has been deployed at the Cabauw Experimental Site for Atmospheric Research (CESAR, www.cesar-observatory.nl) in the Netherlands since 2010. A variety of other instrumentation are also located at CESAR, including Infra-Red radiometers and LIDARs that can determine cloud base height, and by inference, thermodynamic phase. A more recent version of the Cimel, with polarized channels at 440, 500, 675, 870, 1020 and 1640 nm, has been deployed at the NASA Goddard Space Flight Center (GSFC) in suburban Washington, DC. NASA GSFC is the AERONET base of operations, and is also where LIDARs are frequently deployed.

Both versions of the Cimel instrument are primarily employed to measure the DoLP. Since DoLP is insensitive to the orientation of the linearly polarizing filters, the measurement reference plane (as in Eq. 2) does not need to be known. Our simulations, however, indicate that DoLP does not contain information about cloud thermodynamic phase, while Q, defined in the solar principal plane, does. Since reference frame is relevant to the determination of Q, we need to know it accurately for AERONET. Standard operation of AERONET instruments does not require such knowledge, so we attempted to confirm our knowledge of instrument orientation with observations of U. This is equivalent to the method in Li et al. (2009), who identify the reference frame by ensuring the polarization angle, χ, of skylight is consistently 90° from the scattering plane. In the appendix, we explore how polarizing filter orientation knowledge accuracy impacts overall measurement uncertainty.

3.1 Single channel polarimeter site: CESAR

We tested the ability of the single polarized channel AERONET Cimel to determine cloud phase with data from the CESAR site. This site was selected because of the variety and frequency of cloudy conditions encountered in the Netherlands and the availability of coincident data that can indicate cloud thermodynamic phase. A Vaisala LD-40 Ceilometer (which indicates cloud base height, Muenkel et al., 1999, 2002) was positioned at the site. Since cloud drops generally freeze at increased altitudes where

AMTD
7, 11991–12036, 2014

the temperatures falls to somewhere between −20 and −40°C (Riédi et al., 2001; Westbrook and Illingworth, 2011) data from this instrument (along with radiosonde temperature data) can be used to roughly estimate cloud thermodynamic phase.

To analyze these data, we first needed to find the Cimel linearly polarizing filter reference frame. Once known, we could determine the Stokes' vector (Eq. 2) as defined in that frame, and then "rotate" the Stokes vector from its observed frame to the solar principal plane (see Eq. 3.15 in Hansen and Travis, 1974). When defined in the solar principal plane, nearly all polarization should be expressed in the Q Stokes vector element, and U would be minimal (Fig. 2 is an example of this).

Since we had no information about the polarizing filter reference frame, we started with the assumption that they were oriented in the solar principal plane. To test this, we made a scatterplot of Q and U for the entire dataset. If our assumption were correct, we could expect to see no correlation between Q and U, and a wider range of Q values than U values. As we can see from the left-most plot in Fig. 10, this was not the case. If, however, the expected frame of reference is rotated by 16°, we can find a more appropriate relationship between Q and U. This particular angle is most likely due to instrument operation specifics. In this case, the instrument is probably aligned to the solar principal plane while in the "park" mode, and rotates slightly out of the principal plane to avoid a locking mechanism while moving into the zenith viewing mode. We therefore used this reference frame for all subsequent analysis, and performed a similar test for the multiple spectral channel instrument described in the next subsection. The shape of these histograms is also somewhat disturbing. For successful determination of cloud thermodynamic phase, we would hope to see a far wider range of Q than U values. The more compact shape of these histograms indicates the potential for large uncertainties in Q and U.

To illustrate the potential for cloud thermodynamic phase determination, we looked for days in the AERONET dataset at CESAR that had the potential for both ice and water phase clouds. Figure 11 displays one such day, 3 February 2013. The day began with high altitude clouds, with base heights (indicated from LD-40 data in green) at

AMTD
7, 11991–12036, 2014

roughly 5 km, that were eventually replaced with lower clouds with bases heights less than 500 m. A nearby radiosonde found the melting layer height of 0 °C at 570 m, and the homogenous freezing threshold of −40 °C at 7.4 km. Therefore, we expect that the higher altitude clouds were comprised of ice, and the lower clouds of water.

Zenith viewing Cimel observations at CESAR are shown as the blue, black and red dots on Fig. 11. Color indicates the expected cloud phase, where $Q > 0.0001$ are identified as comprised of liquid phase droplets, and $Q < -0.0001$ as ice. Black points were not identified as either phase. Cimel observations are made in bursts of ten measurements. As we can see in Fig. 11, each burst typically had a wide range of values, which based on threshold alone would indicate both liquid and ice phase clouds. Clouds are unlikely to change at such short temporal and spatial scales, so this scatter indicates noise. In an attempt to reduce this noise, we averaged each burst of measurements to create a temporally smoothed product, indicated by diamonds in Fig. 11. On this day, the smoothed product does seem to indicate cloud thermodynamic phase, identifying the early, high altitude clouds as ice, and the later, lower clouds as liquid.

While the analysis of a single day can be informative, observations from the entire dataset provide a more comprehensive and quantitative assessment of this thermodynamic phase detection. Figure 12 shows the two dimensional histograms of observed Q and cloud base height. If the observations are similar to the simulations, we would expect to see a negative correlation. This is not present in either the entire dataset (leftmost plot) or when Q observations are temporally smoothed to reduce noise (rightmost plot).

While disappointing, these results were not entirely unexpected. The Cimel sun photometers were designed to measure the DoLP, not Q, and had an unknown amount of measurement uncertainty. While this analysis is also constrained by appropriateness of our cloud thermodynamic phase proxies, the scatter of Cimel Q observations shown in Fig. 11 shows how those measurements are dominated by noise. Furthermore, we note that the Cimels turn into cloud mode only when the cloud contamination

AMTD
7, 11991–12036, 2014

is unambiguous, which may mean that thin cirrus clouds are not included frequently in these measurements.

3.2 Multiple channel polarimeter site: NASA GSFC

The AERONET Cimel instrument that was deployed at CESAR represents an effort, more than a decade old, to determine aerosol properties from Cimels using polarization (e.g. Vermeulen et al., 2000). These instruments used DoLP and a single channel (870 nm) to find aerosol properties using both direct solar and sky radiance measurements. More recently, Cimels have been developed that have multiple channels. These have been used to retrieve aerosol optical properties with DoLP (Li et al., 2004, 2006, 2007, 2009, 2010, 2013). A portion of these instruments also make zenith mode measurements in the "cloud mode", although polarization data from these measurements are not currently utilized. We assessed a subset of these data acquired at the NASA Goddard Space Flight Center (GSFC) in Greenbelt, Maryland. Figures 13 and 14 illustrate the results of this test, which shows more promise than data collected at the CESAR site (Sect. 3.1). In this case, we used cloud base height from a coincident Micropulse Lidar (MPLnet) (Welton et al., 2001), and temporally smoothed the Cimel data. Since multiple instrument channels were observing polarization, we used the three closest to 870 nm to generate a "multi-spectral" product, where positive of Q values indicate liquid, and negative values indicate ice. The 675, 870 and 1020 nm channels were chosen for this product because of the similarity of the way they express polarimetric cloud scattering (as shown by our simulations, see Fig. 7). Our intent was to reduce random noise by "smoothing" the data, created from the median value of a moving window of all (multispectral) data within an eight minute window.

An example of these data are shown in Fig. 13, which is a case similar to Fig. 11, where high altitude clouds earlier in the day (24 December 2012) were later obscured by lower clouds. Q is lower for the high altitude (and most likely ice) clouds than it is for low altitude (probably liquid) clouds. Data from individual spectral channels show large amounts of scatter within short time windows, indicating that Q from these instruments

AMTD
7, 11991–12036, 2014

contains large (for our purposes) quantities of random noise. In an attempt to reduce this noise, we "smoothed" the combined 675, 870 and 1020 nm data to create the product shown as diamonds on Fig. 13. Like before, we classified this product so that values less than −0.0001 are identified as ice, those greater then 0.0001 as liquid. We can see that what we expect to be ice is indeed identified that way, but liquid clouds are not always properly identified. The smoothed product does have Q values that are larger for liquid than ice clouds, but not large enough to be consistently classified correctly. This points to the possibility of systematic biases in Q, in addition to the random noise the multispectral product is intended to reduce. Indeed, our uncertainty analysis in Appendix A indicates that uncertainty in reference frame knowledge (which we determined with U as shown in Fig. 10) can be important.

Figure 14 is a two dimensional histogram of all data from the month of December 2012 in Greenbelt, and represents a more complete analysis than the single day described in Fig. 13. The negative relationship is also expressed here. If we choose 3 km as a threshold between water and ice clouds, we can use the Q multi-spectral product to correctly identify liquid clouds 78 % of the time, and correctly identify ice clouds 76 % of the time. While this result is promising, it requires further evaluation at more sites and solar geometries, and with additional information from, e.g., ground-based Radar to provide better independent estimates of cloud thermodynamic phase.

4 Discussion

Our simulations show that the direction of linear polarization (as expressed by the sign of the Q element of the Stokes' polarization vector defined in the solar scattering plane) indicates cloud thermodynamic phase in most situations when clouds are observed with passive instruments from below. Liquid phase cloud droplets have positive values of Q, indicating that the linear polarization is parallel to the scattering plane, while ice phase cloud particles have negative Q, meaning that their polarization is perpendicular to the scattering plane.

AMTD
7, 11991–12036, 2014

These conclusions were reached with an atmospheric multiple scattering radiative transfer model, which performed these simulations for a variety of ice particle shapes and several liquid droplet size distributions. We found that the amount of linear polarization (for either liquid or ice) is largest for optically thin clouds, and decreases to nothing for optical depths larger than 10 or 15. Geometries where the scattering angle between the incoming solar path and the observation direction are between 40 and 70° are optimal for thermodynamic phase discrimination. Cloud droplet size distribution has a weak influence on the amount of polarization, but ice particles with extreme aspect ratios (AR) tend to polarize most, and are therefore easiest to distinguish from liquid clouds. Spectral channels with sensitivity in the red or near-infrared are also best for these purposes since liquid droplets polarize strongest at those wavelengths. Finally, while these properties are relatively insensitive to cloud base height or ground surface reflectance, the ability to distinguish ice from liquid clouds diminishes at scattering angles less than 20°. This is also the case if the geometry is such that a halo produced by scattering from pristine ice crystals is observed.

An existing network of ground based sun photometers and radiometers (AERONET, Holben et al., 1998) makes regular observations of clouds (Marshak et al., 2000, 2004; Barker and Marshak, 2001; Chiu et al., 2006, 2010). A subset of these instruments have polarization sensitivity that is used to determine aerosol optical properties (Li et al., 2004, 2006, 2007, 2009, 2010, 2013), but not employed for cloud property retrieval. Our simulations indicate that these data could also be utilized to determine cloud thermodynamic phase, at least for situations where the cloud optical depth is small and geometry is appropriate. This could be an alternate (or complementary) means to determine cloud thermodynamic phase to techniques that use passive infrared observation (e.g. Turner et al., 2003), spectral techniques (e.g. LeBlanc et al., 2014), or active observation of cloud depolarization with lidars and radars (e.g. Sassen (1991), Zrnic and Ryzhkov (1999). Complimentary techniques would be especially useful for techniques that have less accuracy for low cloud optical depths, since the polarization based approach is most accurate for optically thin clouds. Furthermore, this

AMTD
7, 11991–12036, 2014

technique can improve cloud optical depth retrievals that use total (unpolarized) radiation by constraining the retrieval Lookup Table to the appropriate cloud phase (Chiu et al., 2010).

Successful cloud thermodynamic phase determination depends not just on scene conditions, but on instrument capability. Specifically, the accuracy with which Q is determined is key, especially as cloud optical depth increases. For AERONET, calibration methodologies and uncertainty estimates exist for the magnitude of polarization (DoLP), but not for the direction of polarization (Q). It was therefore difficult to know the utility of these techniques without an investigation of AERONET data collected alongside other means of assessing cloud phase, such as by cloud base height.

We tested the ability of polarized AERONET Cimel instruments to determine cloud phase with data from two different sites and with two versions of the polarized Cimel instrument. First, we used data from the CESAR site in the Netherlands. The AERONET Cimel instrument at that site is an older version that is sensitive to polarization at a single channel (870 nm). The first hurdle in analyzing this data was determining the geometrical reference frame for the Stokes polarization vector (Eq. 2). Typically, the polarization from Cimel instruments is represented by the DoLP, which expresses amount of linear polarization and does not have a reference frame. For our purposes, however, we need to know the Stokes vector reference frame, which we determined by minimizing the U vector element. Once we did this, we found a high degree of what appeared to be random noise, which we reduced by smoothing the data within an eight minute window. While this did make it possible to find days where AERONET observations correspond with information about cloud base height (Fig. 11), we were unable to find a systematic relationship between cloud base height and Q (Fig. 12). We performed a similar analysis with data from an AERONET Cimel at GSFC. This instrument is a newer variety that has polarization sensitivity in all channels. Like the instrument at CESAR, we found the polarization reference frame with U, and smoothed the data within an eight minute window. We were able to find a weak relationship between cloud base height and Q (Fig. 14), possibly because we had more data within our eight minute smoothing

AMTD
7, 11991–12036, 2014

window due to the use of three channels. As we have shown with a single day time series (Fig. 13), however, noise and apparent biases still exist.

These results do not indicate with certainty if it is possible to use AERONET Cimel instruments to reliably determine cloud thermodynamic phase. Several steps could be performed to improve the ability of these instruments to determine Q and U, and better characterize their uncertainty. These include:

1. Improving the understanding of the exact instrument geometry while making a polarized cloud measurement. This would provide for a means to determine the polarization frame of reference without the use of U.

2. Characterization of the uncertainty associated with filter orientation and measurement geometry. As we have shown in our uncertainty assessment in Appendix A, knowledge of the reference frame and filter orientation to an uncertainty of tenths of a degree are required to provide an uncertainty less than the threshold of 10^{-4} that we used to discriminate between liquid and ice clouds.

3. Characterization of overall Cimel uncertainty for Q and U, possibly using a modification of the methods described in Li et al. (2010).

4. Modification of the measurement protocol so that clouds are not observed at zenith, but in the solar principal plane at a scattering angle angle of roughly 55°.

5. Modification of the measurement protocol to increase signal to noise and reduce random uncertainty, by using longer integration times or by making bursts of measurements (although it should be noted for this and the previous item that any modification to measurement protocol within AERONET is a complex task).

As part of these efforts, we have purchased a polarization sensitive Cimel instrument to be installed at our home institution, NASA Ames Research Center, at Moffett Field, California. This instrument will be incorporated into AERONET, and also used to address some of the items on the list above. Additionally, we are constructing a simple

AMTD
7, 11991–12036, 2014

linear polarization sensitive instrument for the investigation of this technique, called the Sky Polarization Radiometric Instrument for Test and Evaluation (SPRITE). The instrument, shown under construction in Fig. 15, utilizes high resolution (24 bit) single channel microradiometers designed for ocean optical remote sensing instruments such as the Optical Sensors for Planetary Radiant Energy (OSPREy, Hooker et al., 2012) and the Compact-Optical Profiling System (C-OPS, Morrow et al., 2010). The microradiometers are manufactured by Biospherical Instruments, Inc. and were chosen for their high resolution, compact and modular profile, and low cost. The initial instrument configuration will have a polarization sensitive channel near 870 nm (using three sensors) and a single, non-polarization sensitive channel at or near 440 nm, so that cloud mode observations as in Chiu et al. (2010) can be replicated. If precise calibration and low uncertainty is indeed possible, more channels, and more sophisticated housing, can be added, and the lessons learned can be applied to other instrumentation.

5 Conclusions

When observed from below, cloud thermodynamic phase of clouds is expressed in the direction of linear polarization, although the magnitude (and thus detection) of that polarization is inversely proportional to cloud optical depth. We performed radiative transfer simulations that show this is the case, and tested the range of conditions under which it is most clear. We then investigated polarimetric observations of clouds from the ground, and compared the polarization direction to other indicators of cloud thermodynamic phase to see if our simulations could be confirmed. We did so with data from AERONET, a network of ground based sun photometers and radiometers, a portion of which have polarization sensitivity. We found a large amount of noise and apparent uncertainty in these data, at least for the determination of polarization direction. This was to be expected, since these instruments were primarily designed to produce measurements of the magnitude of polarization, and it is these data that are utilized in retrieval algorithms. We tested instruments with a single (NIR) polarization

AMTD
7, 11991–12036, 2014

sensitive channel and could not find a systematic relationship between polarization direction and cloud base height (our proxy for thermodynamic phase), but we did find a weak relationship with an instrument that has multiple polarization sensitive channels. These results do not conclusively indicate if AERONET instruments can be used to determine cloud thermodynamic phase. We describe a set of recommendations for further activities that will clarify this ambiguity, including a complete characterization and uncertainty analysis of polarimetric direction measurements (see Appendix A), modification of AERONET measurement protocol, and investigation with a prototype instrument expressly designed to identify the limits of polarimetric accuracy and capability.

Appendix A: Uncertainty for instruments with linear polarizers

This appendix describes the measurement systematic uncertainty due to polarizing filter placement and throughput. We limit ourselves to these polarization specific sources of uncertainty, and defer to the far more detailed investigations in publications such as Torres et al. (2014) Li et al. (2010) for other sources of uncertainty.

Both the AERONET Cimel radiometer and the test instrument we have in development use combinations linearly polarizing filters to determine the Stokes' vector. Chandrasekhar's equation for linearly polarized radiation (Chandrasekhar, 1960, Eq. 163) describes the observed signal, $\hat{I}(X)$, for a detector with a linear polarizer oriented at $X°$ from the Stokes' vector reference plane,

$$\hat{I}(X) = \frac{1}{2}[I + Q\cos 2X + U\sin 2X] \quad \text{(A1)}$$

AMTD
7, 11991–12036, 2014

where I, Q and U are Stokes' vector elements. From this, we can derive Eq. (2) for the AERONET Cimel filter configuration,

$$\boldsymbol{I} = \begin{bmatrix} I \\ Q \\ U \end{bmatrix} = \begin{bmatrix} \frac{2}{3}\left(\hat{I}(0°) + \hat{I}(120°) + \hat{I}(240°)\right) \\ \frac{2}{3}\left(2\hat{I}(0°) - \hat{I}(120°) - \hat{I}(240°)\right) \\ \frac{2}{\sqrt{3}}\left(\hat{I}(240°) - \hat{I}(120°)\right) \end{bmatrix}. \quad \text{(A2)}$$

If we include an uncertainty in the placement and knowledge e, in Eq. (A1), we have

$$\hat{I}(X+e) = \frac{1}{2}[I + Q(\cos 2x \cos 2e - \sin 2X \cos 2e) + U(\sin 2X \cos 2e + \cos 2X \sin 2e)]. \quad \text{(A3)}$$

For a sensor with a polarizing filter aligned to the reference plane ($X = 0°$), the difference between expected and observed signal is

$$\sigma_{e0} = |\hat{I}(0+e) - \hat{I}(0)| = \left|\frac{1}{2}(Q\cos 2e - Q + U\sin 2e)\right|. \quad \text{(A4)}$$

For the channels with polarizing filters at other orientations, we have

$$\sigma_{e120} = \left|\frac{1}{4}(Q[1 - \cos 2e + \sqrt{3}\sin 2e] + U[\sqrt{3} - \sqrt{3}\cos 2e - \sin 2e])\right|, \quad \text{(A5)}$$

and

$$\sigma_{e240} = \left|\frac{1}{4}(Q[1 - \cos 2e - \sqrt{3}\sin 2e] + U[-\sqrt{3} + \sqrt{3}\cos 2e - \sin 2e])\right|. \quad \text{(A6)}$$

AMTD
7, 11991–12036, 2014

Additionally, we define f as a fixed, linear uncertainty associated with the efficiency of the polarizing filters. It is identical for each channel, so that $\sigma_{f0} = \sigma_{f120} = \sigma_{f240} = f$

To determine uncertainty in terms of Stokes' vector elements, I, Q and U, we compute the partial derivatives of Eq. (A2),

$$\begin{aligned}
&\frac{\partial I}{\partial \hat{I}(0°)} = \frac{2}{3}, && \frac{\partial I}{\partial \hat{I}(120°)} = \frac{2}{3}, && \frac{\partial I}{\partial \hat{I}(240°)} = \frac{2}{3} \\
&\frac{\partial Q}{\partial \hat{I}(0°)} = \frac{4}{3}, && \frac{\partial Q}{\partial \hat{I}(120°)} = \frac{-2}{3}, && \frac{\partial Q}{\partial \hat{I}(240°)} = \frac{-2}{3} \\
&\frac{\partial U}{\partial \hat{I}(0°)} = 0, && \frac{\partial U}{\partial \hat{I}(120°)} = \frac{2}{\sqrt{3}}, && \frac{\partial U}{\partial \hat{I}(240°)} = \frac{2}{\sqrt{3}}.
\end{aligned} \tag{A7}$$

Using linear error propagation rules, assuming no correlation between e and f, we can write the uncertainty in terms of the individual Stokes' vector elements,

$$\begin{aligned}
\sigma_I^2 &= \frac{4}{9}\left(\sigma_{e0}^2 + \sigma_{e120}^2 + \sigma_{e240}^2 + 3f^2\right) \\
\sigma_Q^2 &= \frac{4}{9}\left(4\sigma_{e0}^2 + \sigma_{e120}^2 + \sigma_{e240}^2 + 6f^2\right) \\
\sigma_U^2 &= \frac{4}{3}\left(\sigma_{e120}^2 + \sigma_{e240}^2 + 2f^2\right).
\end{aligned} \tag{A8}$$

AMTD
7, 11991–12036, 2014

For the I element of the Stokes' vector, this expands to

$$\begin{aligned}\sigma_I^2 =& \frac{4}{3}f^2 + \frac{1}{9}|Q\cos 2e - Q + U\sin 2e|^2 \\ &+ \frac{1}{36}\left|Q\left[1-\cos 2e+\sqrt{3}\sin 2e\right]\right. \\ &\left.+U\left[\sqrt{3}-\sqrt{3}\cos 2e-\sin 2e\right]\right|^2 \\ &+ \frac{1}{36}\left|Q\left[1-\cos 2e-\sqrt{3}\sin 2e\right]\right. \\ &\left.+U\left[-\sqrt{3}+\sqrt{3}\cos 2e-\sin 2e\right]\right|^2, \end{aligned} \tag{A9}$$

which converges to $\frac{4}{3}f^2$ as e becomes small, or if there is no polarization ($Q = U = 0$).

For the Q Stokes' vector element, this is

$$\begin{aligned}\sigma_Q^2 =& \frac{8}{3}f^2 + \frac{4}{9}|Q\cos 2e - Q + U\sin 2e|^2 \\ &+ \frac{1}{36}\left|Q\left[1-\cos 2e+\sqrt{3}\sin 2e\right]\right. \\ &\left.+U\left[\sqrt{3}-\sqrt{3}\cos 2e-\sin 2e\right]\right|^2 \\ &+ \frac{1}{36}\left|Q\left[1-\cos 2e-\sqrt{3}\sin 2e\right]\right. \\ &\left.+U\left[-\sqrt{3}+\sqrt{3}\cos 2e-\sin 2e\right]\right|^2, \end{aligned} \tag{A10}$$

which converges to $\frac{8}{3}f^2$ as e becomes small, or there is no polarization ($Q = U = 0$). This is nearly identical to Eq. (A9), except the first and second term on the right hand side are two and four times as large. Since $I^2 \geq Q^2 + U^2 + V^2$, we can expect $\frac{\sigma_Q^2}{Q^2} \geq \frac{\sigma_I^2}{I^2}$, i.e., the relative error of Q will always be equal to or larger than that of I.

AMTD
7, 11991–12036, 2014

For the U Stokes' vector element, the uncertainty is

$$\sigma_U^2 = \frac{8}{3}f^2 + \frac{1}{12}\left|Q\left[1-\cos 2e+\sqrt{3}\sin 2e\right]\right. \\ \left. +U\left[\sqrt{3}-\sqrt{3}\cos 2e-\sin 2e\right]\right|^2 \\ +\frac{1}{12}\left|Q\left[1-\cos 2e-\sqrt{3}\sin 2e\right]\right. \\ \left. +U\left[-\sqrt{3}+\sqrt{3}\cos 2e-\sin 2e\right]\right|^2, \quad \text{(A11)}$$

which converges to $\frac{8}{3}f^2$ as e becomes small, or there is no polarization ($Q = U = 0$).

Figure A1 expresses the polarimetric uncertainty graphically. As we can see, linear polarizer placement knowledge (e) is important. An uncertainty of $e = 2^\circ$ (black and red) would create uncertainties in I and Q nearly as significant as the results shown in Fig. 4. An uncertainty of $e = 0.1^\circ$ (blue and green) would be more acceptable. The uncertainty estimate in Li et al. (2014), who assume $e = 1^\circ$ but $f = 0$, are roughly between our $e = 0.1^\circ$ and $e = 2^\circ$ results. The uncertainties in I and Q are nearly identical, and differ only for small values of Q when U is not negligible. Although it is not shown in this figure, it should also be noted that the uncertainty in f does not become relevant until it approaches $f \geq 0.01$. Single channel Cimel observations indicate that there is what appears to be noise on the order of 10^{-3} at the CESAR site (see Figs. 11 and 12). Presumably, e and f are systematic uncertainties that would not be expressed as part of this noise, but we mention this to illustrate the general importance of these uncertainty estimates. It would appear that the relative noise contribution to overall uncertainty is large. Assuming a $\sqrt{n}$ uncertainty reduction when averaging, reducing noise from 10^{-3} to 10^{-4} would require averages of 100 measurements.

Acknowledgements. This research was supported by Science Innovation Fund (SIF) grants at NASA Ames Research Center (Knobelspiesse, Dunagan, van Diedenhoven) and NASA Goddard Space Flight Center (Marshak, Holben). Thanks to John Livingston for his help finding

AMTD
7, 11991–12036, 2014

validation data, and members of the NASA Ames Sunphotometer-Satellite Team for informally reviewing this manuscript. LD-40 data from the CESAR site, and Radiosonde data from De Bilt, are provided courtesy of the Koninklijk Nederlands Meteorologisch Instituut (KNMI), with the assistance of Henk Klein Baltink. Radiosonde data from Sterling, Virginia are from the National Weather Service. We thank the members of the AERONET team at the NASA Goddard Space Flight Center for providing instrument calibration, data processing and field measurement support.

References

Baran, A. J.: A review of the light scattering properties of cirrus, J. Quant. Spectrosc. Ra., 110, 1239–1260, 2009. 11995, 11999

Barker, H. W. and Marshak, A.: Inferring optical depth of broken clouds above green vegetation using surface solar radiometric measurements, J. Atmos. Sci., 58, 2989–3006, 2001. 11993, 12007

Bi, L., Yang, P., Liu, C., Yi, B., Baum, B. A., van Diedenhoven, B., and Iwabuchi, H.: Assessment of the accuracy of the conventional ray-tracing technique: implications in remote sensing and radiative transfer involving ice clouds, J. Quant. Spectrosc. Ra., 146, 158–174, 2014. 11999

Campos, E. F., Ware, R., Joe, P., and Hudak, D.: Monitoring water phase dynamics in winter clouds, Atmos. Res., 147, 86–100, 2014. 12001

Chandrasekhar, S.: Radiative Transfer, Dover Publications, Inc., New York, NY, 1960. 11996, 12011

Chiu, J. C., Marshak, A., Knyazikhin, Y., Wiscombe, W. J., Barker, H. W., Barnard, J. C., and Luo, Y.: Remote sensing of cloud properties using ground-based measurements of zenith radiance, J. Geophys. Res.-Atmos., 111, D16201, doi:10.1029/2005JD006843, 2006. 11993, 12000, 12007

Chiu, J. C., Huang, C.-H., Marshak, A., Slutsker, I., Giles, D. M., Holben, B. N., Knyazikhin, Y., and Wiscombe, W. J.: Cloud optical depth retrievals from the Aerosol Robotic Network (AERONET) cloud mode observations, J. Geophys. Res., 115, D14202, doi:10.1029/2009JD013121, 2010. 11993, 12000, 12007, 12008, 12010

Davis, A. B. and Marshak, A.: Space-time characteristics of light transmitted through dense clouds: a Green's function analysis, J. Atmos. Sci., 59, 2713–2727, 2002. 11998

AMTD
7, 11991–12036, 2014

de Haan, J., Bosma, P., and Hovenier, J.: The adding method for multiple scattering calculations of polarized light, Astron. Astrophys., 183, 371–391, 1987. 11994, 11996

Hansen, J. and Travis, L.: Light scattering in planetary atmospheres, Space Sci. Rev., 16, 527–610, 1974. 11994, 11997, 12003

Holben, B., Kaufman, Y., Eck, T., Slutsker, I., Tanre, D., Buis, J., Setzer, A., Vermote, E., and Reagan, J.: AERONET – a federated instrument network and data archive for aerosol characterization, Remote Sens. Environ., 66, 1–16, 1998. 11993, 12001, 12007

Hooker, S., Benhard, G., Morrow, J., Booth, C., Comer, T., Lind, R., and Quang, V.: Optical Sensors for Planetary Radiant Energy (OSPREy): calibration and validation of current and next-generation NASA missions, Tech. Rep. TM-2012-215872, National Aeronautics and Space Administration, http://ntrs.nasa.gov (last access: 1 December 2014), 2012. 12010

IPCC: Climate Change 2013 – The Physical Science Basis: Contribution of the Working Group I to the Fifth Assessment Report of the IPCC, Cambridge University Press, New York, NY, 2013. 11993

Kawata, Y.: Circular polarization of sunlight reflected by planetary atmospheres, Icarus, 33, 217–232, 1978. 11996

Knobelspiesse, K., Cairns, B., Schaaf, C., Schmid, B., and Román, M.: Surface BRDF estimation from an aircraft compared to MODIS and ground estimates at the Southern Great Plains site, J. Geophys. Res., 113, 1–21, 2008. 11995, 12021, 12022

LeBlanc, S. E., Pilewskie, P., Schmidt, K. S., and Coddington, O.: A generalized method for discriminating thermodynamic phase and retrieving cloud optical thickness and effective radius using transmitted shortwave radiance spectra, Atmos. Meas. Tech. Discuss., 7, 5293–5346, doi:10.5194/amtd-7-5293-2014, 2014. 12001, 12007

Li, L., Li, Z., Li, K., Blarel, L., and Wendisch, M.: A method to calculate Stokes parameters and angle of polarization of skylight from polarized CIMEL sun/sky radiometers, J. Quant. Spectrosc. Ra., 149, 334–346, doi:10.1016/j.jqsrt.2014.09.003, 2014. 12015

Li, Z., Goloub, P., Devaux, C., Gu, X., Qiao, Y., Zhao, F., and Chen, H.: Aerosol polarized phase function and single-scattering albedo retrieved from ground-based measurements, Atmos. Res., 71, 233–241, 2004. 11994, 12005, 12007

Li, Z., Goloub, P., Devaux, C., Gu, X., Deuze, J.-L., Qiao, Y., and Zhao, F.: Retrieval of aerosol optical and physical properties from ground-based spectral, multi-angular, and polarized sunphotometer measurements, Remote Sens. Environ., 101, 519–533, 2006. 11994, 12005, 12007

AMTD
7, 11991–12036, 2014

Li, Z., Goloub, P., Blarel, L., Damiri, B., Podvin, T., and Jankowiak, I.: Dust optical properties retrieved from ground-based polarimetric measurements, Appl. Optics, 46, 1548–1553, 2007. 11994, 12005, 12007

Li, Z., Goloub, P., Dubovik, O., Blarel, L., Zhang, W., Podvin, T., Sinyuk, A., Sorokin, M., Chen, H., Holben, B., Tanré, D., Canini, M., and Buis, J.-P.: Improvements for ground-based remote sensing of atmospheric aerosol properties by additional polarimetric measurements, J. Quant. Spectrosc. Ra., 110, 1954–1961, 2009. 11994, 12002, 12005, 12007

Li, Z., Blarel, L., Podvin, T., Goloub, P., and Chen, L.: Calibration of the degree of linear polarization measurement of polarized radiometer using solar light, Appl. Optics, 49, 1249–1256, 2010. 11994, 12005, 12007, 12009, 12011

Li, Z., Gu, X., Wang, L., Li, D., Xie, Y., Li, K., Dubovik, O., Schuster, G., Goloub, P., Zhang, Y., Li, L., Ma, Y., and Xu, H.: Aerosol physical and chemical properties retrieved from ground-based remote sensing measurements during heavy haze days in Beijing winter, Atmos. Chem. Phys., 13, 10171–10183, doi:10.5194/acp-13-10171-2013, 2013. 11994, 12005, 12007

Macke, A., Mueller, J., and Raschke, E.: Single scattering properties of atmospheric ice crystals, J. Atmos. Sci., 53, 2813–2825, 1996. 11994, 11995, 12026

Magee, N. B., Miller, A., Amaral, M., and Cumiskey, A.: Mesoscopic surface roughness of ice crystals pervasive across a wide range of ice crystal conditions, Atmos. Chem. Phys. Discuss., 14, 8393–8418, doi:10.5194/acpd-14-8393-2014, 2014. 11999

Marshak, A., Knyazikhin, Y., Davis, A., Wiscombe, W., and Pilewskie, P.: Cloud-vegetation interaction: use of normalized difference cloud index for estimation of cloud optical thickness, Geophys. Res. Lett., 27, 1695–1698, 2000. 11993, 12007

Marshak, A., Knyazikhin, Y., Evans, K., and Wiscombe, W.: The “RED versus NIR” plane to retrieve broken-cloud optical depth from ground-based measurements, J. Atmos. Sci., 61, 1911–1925, 2004. 11993, 12007

Martins, J. V., Marshak, A., Remer, L. A., Rosenfeld, D., Kaufman, Y. J., Fernandez-Borda, R., Koren, I., Correia, A. L., Zubko, V., and Artaxo, P.: Remote sensing the vertical profile of cloud droplet effective radius, thermodynamic phase, and temperature, Atmos. Chem. Phys., 11, 9485–9501, doi:10.5194/acp-11-9485-2011, 2011. 12001

Morrow, J., Hooker, S., Booth, C., Bernhard, G., Lind, R., and Brown, J.: Advances in measuring the Apparent Optical Properties (AOPs) of optically complex waters, Tech. Rep. TM-2010-215856, National Aeronautics and Space Administration, ntrs.nasa.gov, 2010. 12010

AMTD
7, 11991–12036, 2014

Muenkel, C., Leiterer, U., and Dier, H.-D.: Scanning the troposphere with a low-cost eye-safe lidar, in: Industrial Lasers and Inspection (EUROPTO Series), International Society for Optics and Photonics, 2–9, 1999. 12002

Muenkel, C., Leiterer, U., and Dier, H.-D.: Affordable lidar for atmospheric aerosol and cloud studies, in: International Symposium on Optical Science and Technology, International Society for Optics and Photonics, 198–206, 2002. 12002

Pfalzgraff, W. C., Hulscher, R. M., and Neshyba, S. P.: Scanning electron microscopy and molecular dynamics of surfaces of growing and ablating hexagonal ice crystals, Atmos. Chem. Phys., 10, 2927–2935, doi:10.5194/acp-10-2927-2010, 2010. 11999

Riédi, J., Goloub, P., and Marchand, R. T.: Comparison of POLDER cloud phase retrievals to active remote sensors measurements at the ARM SGP site, Geophys. Res. Lett., 28, 2185–2188, 2001. 12003

Sassen, K.: The polarization lidar technique for cloud research: a review and current assessment, B. Am. Meteorol. Soc., 72, 1848–1866, 1991. 12001, 12007

Sassen, K., Zhu, J., and Benson, S.: Midlatitude cirrus cloud climatology from the Facility for Atmospheric Remote Sensing. IV. Optical displays, Appl. Optics, 42, 332–341, 2003. 11999

Shcherbakov, V.: Why the 46° halo is seen far less often than the 22° halo?, J. Quant. Spectrosc. Ra., 124, 37–44, 2013. 12000

Shupe, M. D., Uttal, T., and Matrosov, S. Y.: Arctic cloud microphysics retrievals from surface-based remote sensors at SHEBA, J. Appl. Meteorol., 44, 1544–1562, 2005. 12001

Torres, B., Dubovik, O., Toledano, C., Berjon, A., Cachorro, V. E., Lapyonok, T., Litvinov, P., and Goloub, P.: Sensitivity of aerosol retrieval to geometrical configuration of ground-based sun/sky radiometer observations, Atmos. Chem. Phys., 14, 847–875, doi:10.5194/acp-14-847-2014, 2014. 12011

Turner, D. D., Ackerman, S., Baum, B., Revercomb, H. E., and Yang, P.: Cloud phase determination using ground-based AERI observations at SHEBA, J. Appl. Meteorol., 42, 701–715, 2003. 12001, 12007

Um, J. and McFarquhar, G. M.: Single-scattering properties of aggregates of bullet rosettes in cirrus, J. Appl. Meteorol. Clim., 46, 757–775, 2007. 11995

Um, J. and McFarquhar, G. M.: Single-scattering properties of aggregates of plates, Q. J. Roy. Meteor. Soc., 135, 291–304, 2009. 11995

van Diedenhoven, B.: The prevalence of the 22° halo in cirrus clouds, J. Quant. Spectrosc. Ra., 146, 475–479, doi:10.1016/j.jqsrt.2014.01.012, 2014. 11999, 12000

AMTD
7, 11991–12036, 2014

van Diedenhoven, B., Cairns, B., Geogdzhayev, I. V., Fridlind, A. M., Ackerman, A. S., Yang, P., and Baum, B. A.: Remote sensing of ice crystal asymmetry parameter using multi-directional polarization measurements – Part 1: Methodology and evaluation with simulated measurements, Atmos. Meas. Tech., 5, 2361–2374, doi:10.5194/amt-5-2361-2012, 2012. 11999

van Diedenhoven, B., Cairns, B., Fridlind, A. M., Ackerman, A. S., and Garrett, T. J.: Remote sensing of ice crystal asymmetry parameter using multi-directional polarization measurements – Part 2: Application to the Research Scanning Polarimeter, Atmos. Chem. Phys., 13, 3185–3203, doi:10.5194/acp-13-3185-2013, 2013. 11999

van Diedenhoven, B., Ackerman, A. S., Cairns, B., and Fridlind, A. M.: A flexible parameterization for shortwave optical properties of ice crystals, J. Atmos. Sci., 71, 1763–1782, 2014. 11995

Vermeulen, A., Devaux, C., and Herman, M.: Retrieval of the scattering and microphysical properties of aerosols from ground-based optical measurements including polarization. I. Method, Appl. Optics, 39, 6207–6220, 2000. 12005

Welton, E. J., Campbell, J. R., Spinhirne, J. D., and Scott III, V. S.: Global monitoring of clouds and aerosols using a network of micropulse lidar systems, in: Second International Asia-Pacific Symposium on Remote Sensing of the Atmosphere, Environment, and Space, International Society for Optics and Photonics, 151–158, 2001. 12005

Westbrook, C. and Illingworth, A.: Evidence that ice forms primarily in supercooled liquid clouds at temperatures $> -27\,^{\circ}C$, Geophys. Res. Lett., 38, L14808, doi:10.1029/2011GL048021, 2011. 12003

Zrnic, D. S. and Ryzhkov, A. V.: Polarimetry for weather surveillance radars, B. Am. Meteorol. Soc., 80, 389–406, 1999. 12007

AMTD
7, 11991–12036, 2014

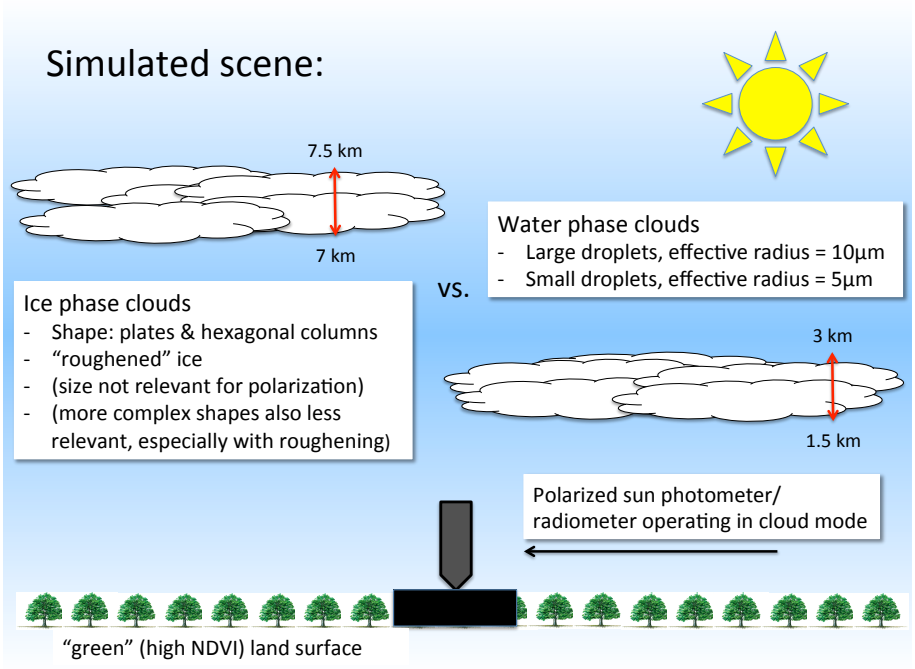

Figure 1. Cartoon illustrating the simulated scene. Sky radiances were generated for a variety of Solar Zenith Angles (15, 30, 45 and 60°), Cloud Optical Depths (2.5, 5, 7.5, 10, 15, 20 and 30) and ice particle or cloud droplet types (see Sect. 2). Surface reflectance was provided by observations of high Normalized Difference Vegetation Index (NDVI) from late summer in central Oklahoma (Knobelspiesse et al., 2008).

AMTD
7, 11991–12036, 2014

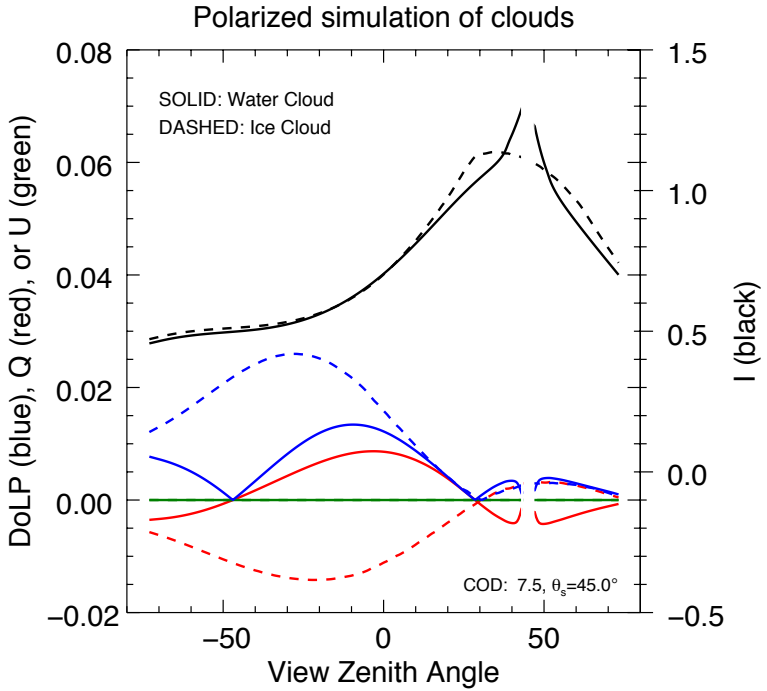

Figure 2. Simulated ground observation of a liquid and ice phase cloud in the solar principal plane. The simulation wavelength was 870 nm, COD was 7.5, and Solar Zenith Angle 45°. The water cloud (solid lines) had droplets with an effective radius of 10 µm, while the ice cloud (dashed lines) was comprised of crystals with an aspect ratio of 20 and roughness parameter of 0.4. Both simulations used an isotropic surface reflectance of 0.391, which was observed at 870 nm for a vegetated surface by Knobelspiesse et al. (2008). DoLP (blue), *Q* (red) and *U* (green) are expressed with the axis on the left, while *I* (black) the axis on the right. Values within 2° of the incoming solar direction (45°) were omitted for graphical clarity.

AMTD
7, 11991–12036, 2014

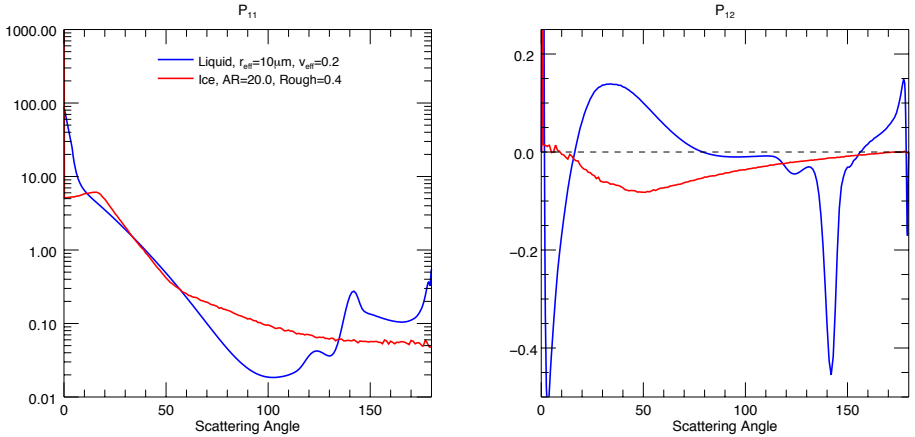

Figure 3. Example P_{11} and P_{12} phase matrix elements for water (blue) and ice (red) clouds. The P_{11} element, which generates scattering from unpolarized radiation for the *I* Stokes' vector component, is quite similar for water and ice clouds at typical scattering angles for ground observation (less than 70°). Conversely, the P_{12} element, which generates scattering from unpolarized radiation for the *Q* Stokes' vector component, has a different sign for most observable scattering angles. As we have seen in Fig. 2, this sign difference is maintained with multiple scattering. Note that both P_{11} and P_{12} are strongly forward scattering, but that this peak is beyond the plotting range for P_{12}.

AMTD
7, 11991–12036, 2014

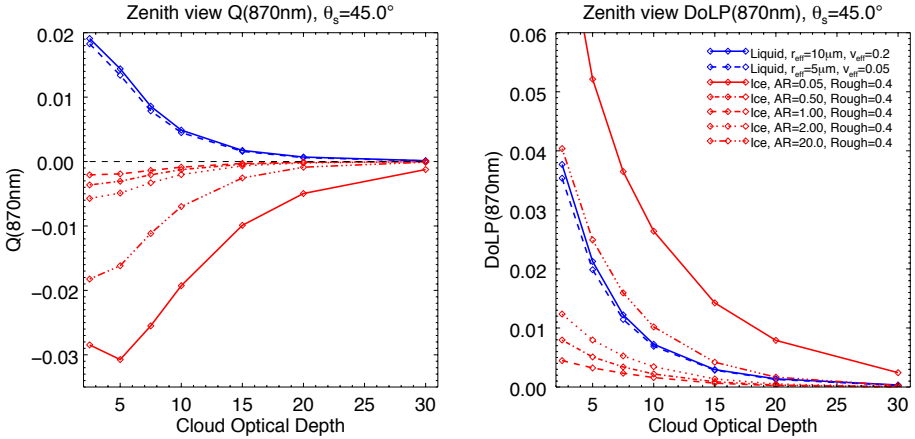

Figure 4. Simulated Q (left) and DoLP (right) for liquid (blue) and ice (red) phase clouds observed from the ground by a polarimeter observing in the zenith direction at 870 nm and with a Solar Zenith Angle of $\theta_s = 45^\circ$.

AMTD
7, 11991–12036, 2014

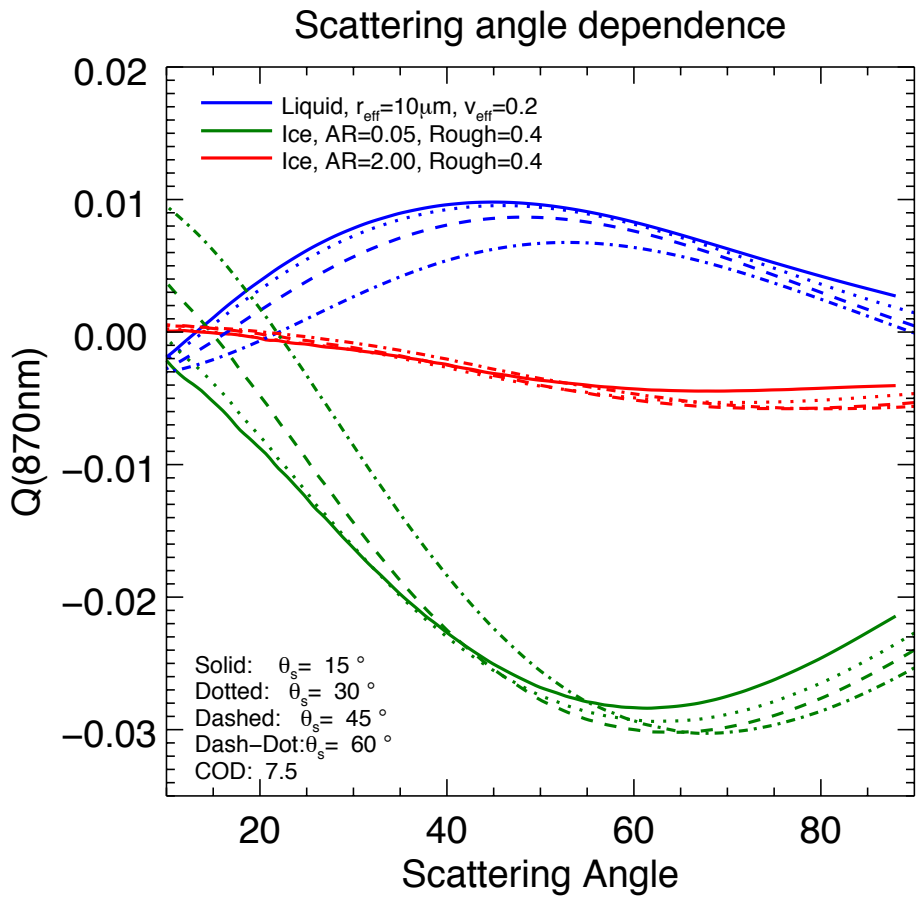

Figure 5. Simulated *Q* as a function of scattering angle (defined as the angle from the solar incidence direction) for a liquid cloud (blue), ice cloud with an extreme aspect ratio (green) and an ice cloud with a more compact aspect ratio (red). The line style indicates the simulation solar zenith angle.

AMTD
7, 11991–12036, 2014

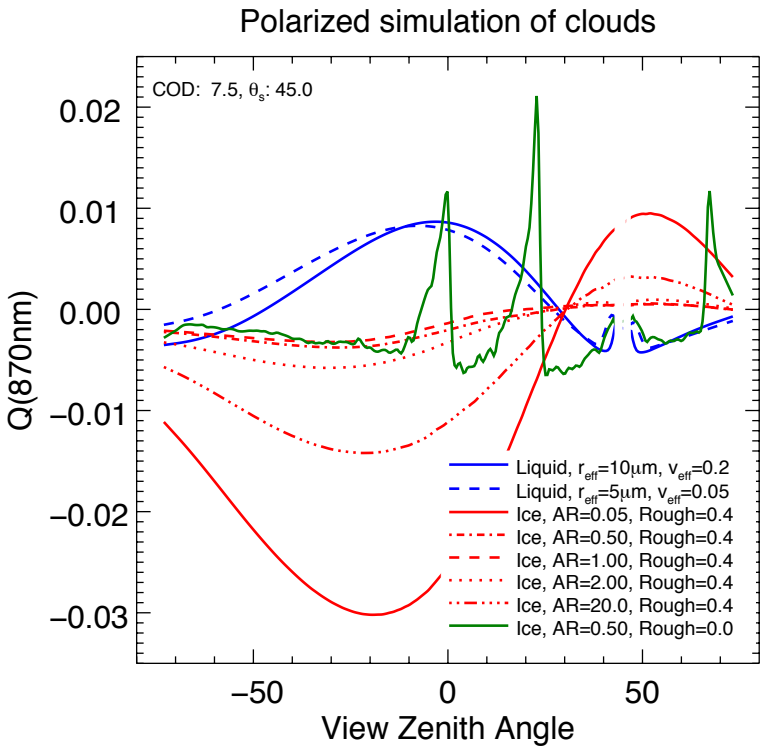

Figure 6. Simulated *Q* with respect to view zenith angle for liquid (blue) and ice clouds, including an ice cloud comprised of pristine crystals (green, roughened crystal clouds are shown in red). The roughness factor, which is zero for pristine crystals and increases with surface facet randomization, is defined according to Macke et al. (1996). Both the 22 and 46° halos (at zenith angles of roughly 23 and 67° for the 22° halo, and 0° for the 46° halo) are clear for the pristine ice crystal cloud.

AMTD
7, 11991–12036, 2014

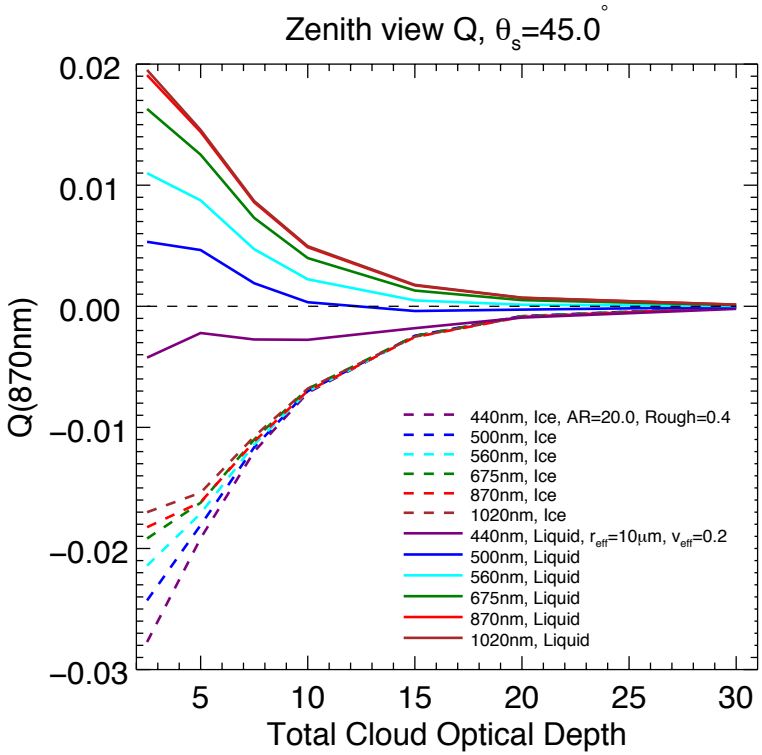

Figure 7. Spectral dependance of simulated Q as a function of cloud optical depth. The linear polarization of liquid clouds (r_{eff} = 20 µm, v_{eff} = 0.2 shown here) changes significantly for different wavelengths. Q is smaller as wavelength decreases, and the shortest wavelength, 440 nm, is negative. Ice clouds are more uniform for the various simulated spectral channels. Like liquid clouds, ice clouds (AR = 20, Roughness = 0.4 shown here) have more negative values of Q as wavelength is decreased.

AMTD
7, 11991–12036, 2014

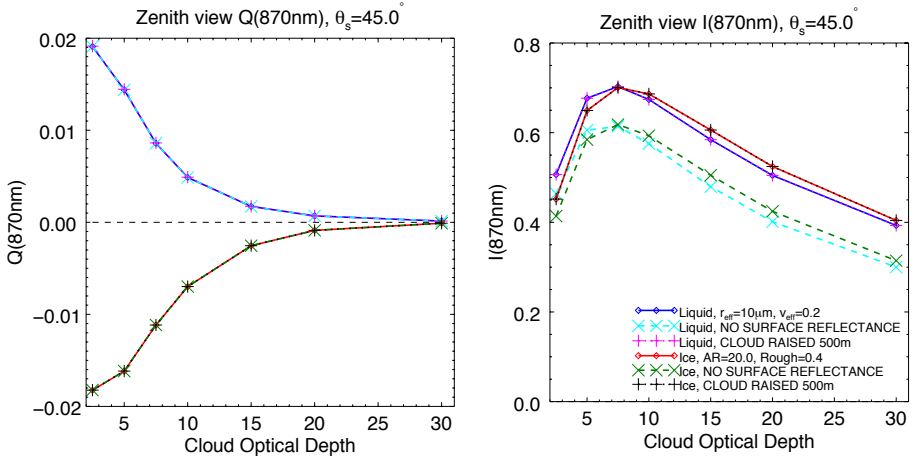

Figure 8. Simulated *Q* (left) and *I* (right) for liquid (blue, cyan, magenta) and ice (red, green, black) phase clouds observed from the ground by a polarimeter observing in the zenith direction at 870 nm and with a Solar Zenith Angle of $\theta_s = 45^\circ$. Both the liquid and ice clouds were simulated with different surfaces reflectances (cyan and green) and altitudes (magenta and black). The left most plot illustrates the lack of sensitivity to these changes for *Q*, while sensitivity to surface reflectance for *I* is shown at right. Cloud base height does not strongly affect either *Q* or *I*.

AMTD
7, 11991–12036, 2014

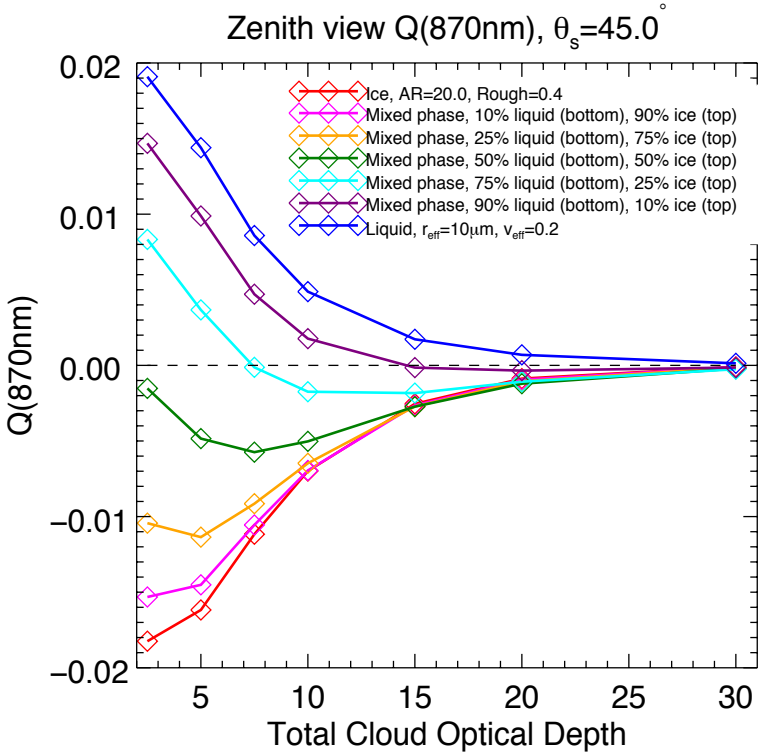

Figure 9. Nadir observed Q (870 nm) at varying COD's for an ice phase cloud (red), liquid phase cloud (blue), and mixed phased clouds. The mixed phase clouds have the liquid phase on the bottom and ice on the top, mixed in percentages of total COD. The simulated Solar Zenith Angle was $\theta_s = 45^\circ$.

AMTD
7, 11991–12036, 2014

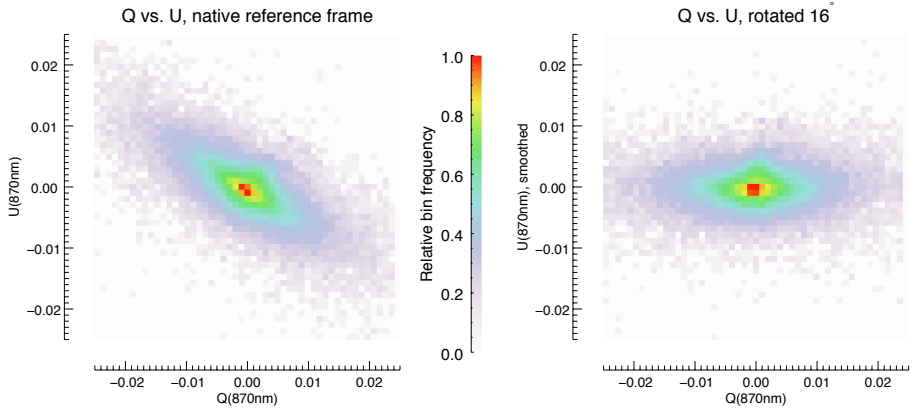

Figure 10. Two dimensional histograms of Q vs. U for the AERONET Cimel instrument operating at the CESAR site from 9 June 2010 to 15 March 2013. The histogram at left is for Q and U defined assuming the instrument linear polarizers are aligned with the solar principal plane. Scattering theory for randomly oriented particles indicates that U should be minimized and Q maximized when they are defined with respect to the solar principal plane. Since this is not the case, we found that only by rotating the assumed polarizing filter orientation by 16° could we pinpoint the appropriate distribution of Q and U, shown at right.

AMTD
7, 11991–12036, 2014

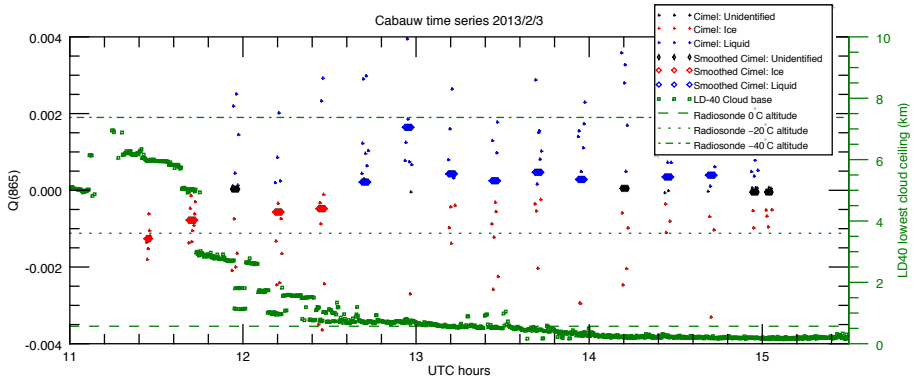

Figure 11. Cimel polarized zenith radiance and Vaisala LD-40 Ceilometer data from 3 February 2013, at the CESAR site. Local noon was at UTC = 13:00. Ceilometer data (green) indicate high altitude (ice) clouds until about UTC 12:00, when low altitude (water) clouds appeared. Cimel data (tagged in blue for liquid, red for ice, black otherwise) show little indication of cloud phase. Smoothed data (averages within a ten minute moving window) do a slightly better job of indicating cloud phase, and are indicated by blue, red and black diamonds. A radiosonde launched at EHDB De Bilt, roughly 25 km north east of CESAR, found temperatures of 0 °C at 570 m, −20 °C at 3600 m, and −40 °C at roughly 7.4 km.

AMTD
7, 11991–12036, 2014

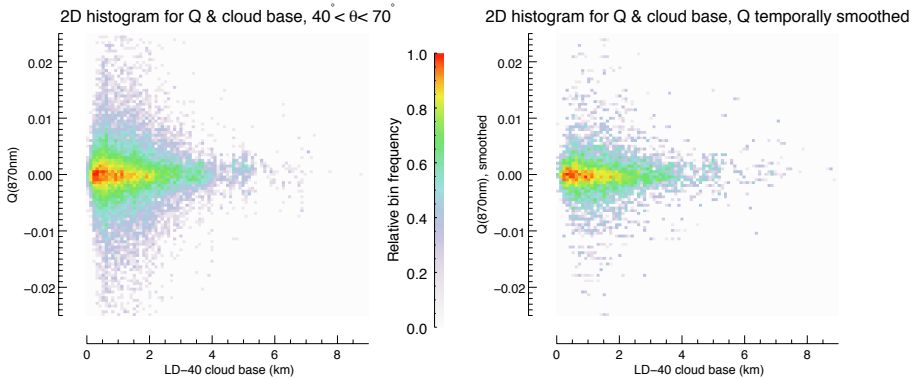

Figure 12. Two dimensional histograms of the single channel AERONET *Q* compared to cloud base height determined by the LD-40 ceilingometer at the CESAR site. Original AERONET data are shown at left, while the values at the right represent temporally smoothed values. To clarify display, *Q* with an absolute value less than 0.0001 were removed. For the original data, 50 % were larger than this threshold, while 46 % were less. For the smoothedl data, 48 % were larger than this threshold, while 45 % were less. Data were gathered between 9 June 2010 and 28 February 2013.

AMTD
7, 11991–12036, 2014

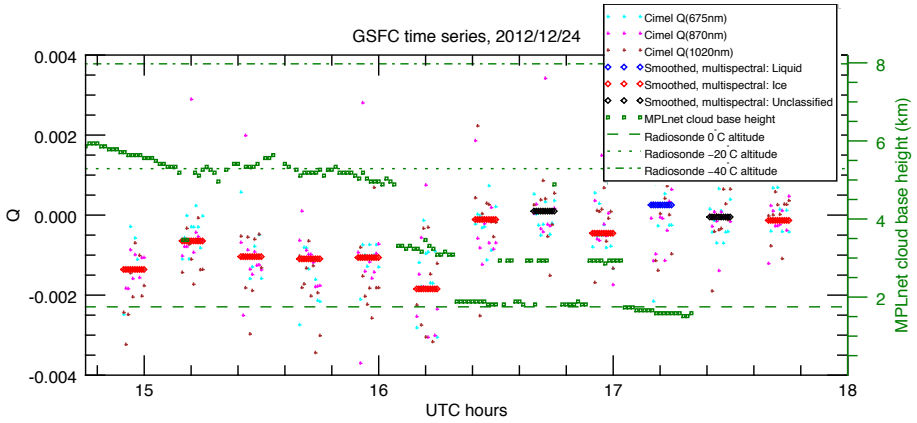

Figure 13. Cimel polarized radiance and MPLnet cloud base height from 24 December 2012 at the NASA GSFC site. Local noon was at UTC = 17:00. Lidar cloud base heights (green) indicate high altitude clouds before roughly 16:00, followed by low altitude clouds. Cimel nadir observations of Q at 675 nm (cyan), 870 nm (magenta) and 1020 nm (brown) show a high degree of scatter but generally more negative values during high altitude cloud cover. A radiosonde launched at Sterling, Virginia (Washington Dulles International Airport), roughly 50 km West of NASA GSFC, found temperatures of 0 °C a 1750 m, −20 °C at 5.3 km and −40 °C at roughly 8 km, indicating that the lowest clouds were almost certainly comprised of liquid droplets, which the higher clouds were probably comprised of ice particles. A multispectral smoothed product, representing the median of a moving window of data from all three channels taken within eight minutes of the window center, are shown as diamonds. They are classified in the same way as were the CESAR data, where values less than −0.0001 are identified as ice (red), larger than 0.0001 as liquid (blue) and unclassified (black) between those values.

AMTD
7, 11991–12036, 2014

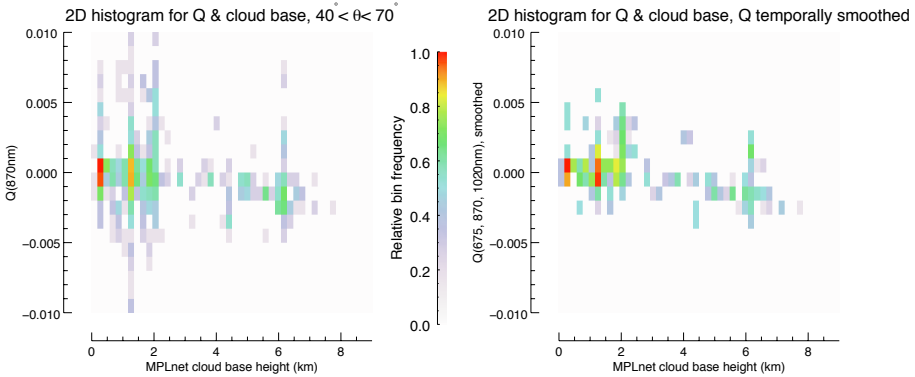

Figure 14. Two dimensional histograms of Q (870 nm) with respect to MPLnet cloud base height (left) and the smoothed multispectral (675, 870 and 102 nm) Q product vs. the same (right) with the multi wavelength Cimel instrument at NASA GSFC, for December 2012. The apparent inverse relationship between Q and cloud base height is consistent with the simulations in Sect. 2. If we choose 3 km as a threshold between water and ice clouds, we can use the temporally smoothed Q multi-spectral product to correctly identify liquid clouds 78 % of the time, and correctly identify ice clouds 76 % of the time.

AMTD
7, 11991–12036, 2014

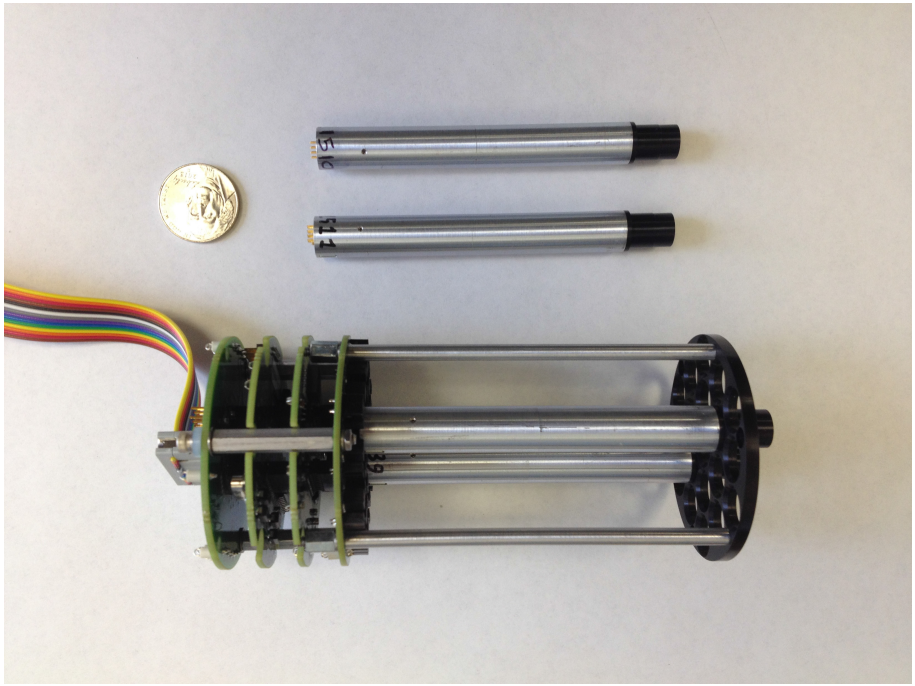

Figure 15. SPRITE, a prototype instrument for the investigation of the polarimetric cloud thermodynamic phase determination technique. Microradiometers manufactured by Biospherical Instruments, Inc. (below) will be used with a modular housing (above) that allows for up to 19 individual microradiometers.

AMTD
7, 11991–12036, 2014

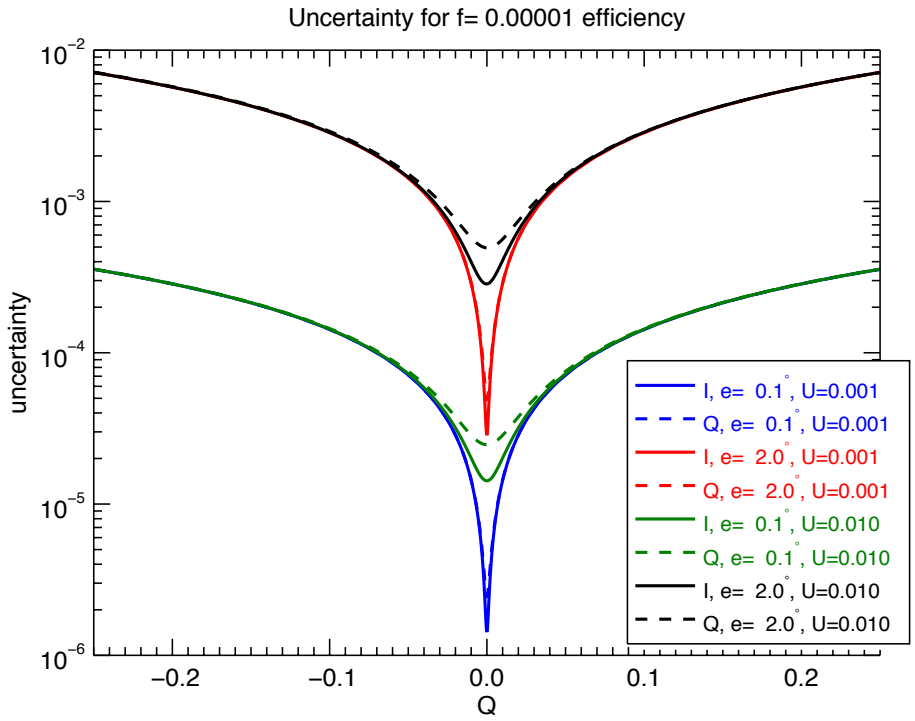

Figure A1. Polarimetric uncertainty in reflectance units for a scene with $I = 0.5$, $\theta_s = 45^\circ$ and $f = 10^{-5}$, and various values of Q, U and e.

AMTD
7, 11991–12036, 2014